Article

High-Yield and Quantitative Purification Method for HIV Which Minimizes Forces Applied to Virions Utilized to Investigate Maturation of HIV-1 via Cryo-Electron Tomography

Benjamin Preece [1,2,†], Wiley Peppel [1,2,†], Rodrigo Gallegos [1,2], Gillian Ysassi [1,2], Gabriel Clinger [1,2], Nicole Bohn [1,2], Broti Adhikary [3], Luiza Mendonça [3], David Belnap [4,5], Michael Vershinin [6] and Saveez Saffarian [1,2,4,7,*]

1 Department of Physics and Astronomy, University of Utah, Salt Lake City, UT 84112, USA
2 Center for Cell and Genome Science, University of Utah, Salt Lake City, UT 84112, USA
3 Department of Biochemistry, Molecular Biology and Biophysics, University of Minnesota, Minneapolis, MN 55455, USA
4 School of Biological Sciences, University of Utah, Salt Lake City, UT 84112, USA
5 Department of Biochemistry, University of Utah, Salt Lake City, UT 84112, USA
6 Department of Chemistry and Physical Sciences, Nicholls State University, Thibodaux, LA 70301, USA
7 Department of Molecular and Cell Biology, University of California, Berkeley, CA 94720, USA
* Correspondence: saveez.saffarian@berkeley.edu
† These authors contributed equally to this work.

Abstract: HIV is a lentivirus characterized by its cone shaped mature core. Visualization and structural examination of HIV requires the purification of virions to high concentrations. The yield and integrity of these virions are crucial for ensuring a uniform representation of all viral particles in subsequent analyses. In this study, we present a method for the purification of HIV virions which minimizes the forces applied to virions while maximizing the efficiency of collection. This method, which relies on virion sedimentation simulations, allows us to capture between 1000 and 5000 HIV virions released from individual HEK293 cells after transfection with the NL4.3 HIV backbone. We utilized this approach to investigate HIV core formation from several constructs: pNL4-3(RT:D_{185}A&D_{186}A) with an inactive reverse transcriptase, NL4.3(IN: V_{165}A&R_{166}A) with a type-II integrase mutation, and NL4.3(Ψ: Δ(105–278)&Δ(301–332)) featuring an edited Ψ packaging signal. Notably, virions from NL4.3(Ψ: Δ(105–278)&Δ(301–332)) displayed a mixed population, comprising immature virions, empty cores, and cores with detectable internal density. Conversely, virions derived from NL4.3(IN: V_{165}A&R_{166}A) exhibited a type II integrase mutant phenotype characterized by empty cores and RNP density localized around the cores, consistent with previous studies. In contrast, virions released from pNL4-3(RT:D_{185}A&D_{186}A) displayed mature cores containing detectable RNP density. We suggest that the sedimentation simulations developed in this study can facilitate the characterization of enveloped viruses.

Keywords: HIV; infectivity; Gag-Pol; gRNA

1. Introduction

Human immunodeficiency virus (HIV) is a complex retrovirus which replicates in CD4+ T cells and macrophages, destroying the ability of the body to fight other infections and causing acquired immunodeficiency syndrome (AIDS). There are two types of HIV: HIV-1 originated from the SIV of the chimpanzee and has spread globally [1,2], while HIV-2 originated from the SIV of the sooty mangabey and is relatively limited to the African

continent [2,3]. Historically, purification protocols originally developed for Rous sarcoma virus (RSV) and Avian myeloblastosis virus (AMV) have been widely used to purify all retroviruses, including HIV-1 and HIV-2, due to their similar density (1.16 g/mL) and particle size (~150 nm in diameter) [4]. The most common purification methods are as follows. The virus is first collected by centrifugation of the growth medium over a sucrose or OptiPrep solution cushion, where OptiPrep is a 60/40 solution of Iodixanol. The resulting pellet is redissolved and the particles separated over a sucrose density gradient [4,5], OptiPrep velocity gradient [6], OptiPrep density gradient [7], or OptiPrep step gradient [8]. After extraction from the gradients, the virus is sedimented again and resuspended in the final buffer, suitable for further analysis. Due to their pelleting and resuspension steps, these methods are ideal for purification of virions at the very high densities required for cryo electron microscopy. Retroviral purification has also been developed specifically for Lentiviral vectors [9], and since lentiviral preps do not require the degree of concentration required for cryo electron microscopy, lentiviral vectors are commonly purified using chromatography [10].

The primary motivation for our study was to update a purification protocol for HIV virions to capture all virions released by producer cells with minimal structural damage by calculating and minimizing the forces encountered by virions during purification. Cryo-electron tomography and single particle electron microscopy offer powerful techniques to visualize the protein–protein and protein–lipid contacts within HIV virions [5,11–15]. The goal is to purify a majority of the virions released from producer cells so all phenotypes are captured in analysis irrespective of the variation in their structural integrity.

HIV-1 virion assembly initiates on the plasma membrane through interactions between specialized lipids, specifically PiP_2 [16–18], HIV Gag proteins, and the Ψ packaging signal of the viral genomic RNA (gRNA) [19–25]. During its assembly, the nascent virion incorporates HIV gp40/gp120 trimers, Gag-Pol, and a number of HIV accessory proteins [26,27]. The released virions are immature, with a distinct lattice of Gag molecules underpinning the inner leaflet of the virions [11,12]. HIV maturation is catalyzed by the active protease dimer [28], and maturation results in the formation of a conical core made from HIV Gag capsid proteins (CA), encompassing two copies of HIV gRNA bound to Gag nucleocapsid (NC) along with the reverse transcriptase and integrase enzymes (RNP) [2,13,14]. After fusion of the viral membrane with the next host, the integrity of the mature core is essential for delivery of the HIV RNP to the nucleus of the next host [29,30], allowing for integration of the viral DNA into the genome of the target cell. The molecular mechanism of HIV maturation is intricate and therefore offers a good target for the development of next generation antivirals [27,31]. HIV assembly, release, and maturation are complex processes and more details can be found in extensive reviews [21,26,31–34].

A major enzyme within HIV virions is the reverse transcriptase, which functions as a heterodimer, which forms after processing of Gag-Pol and release of the reverse transcriptase monomers within the lumen of HIV virions. The reverse transcriptase is essential for transcribing a single DNA molecule from the two gRNA templates embedded in each virion [2]. The $_{183}YMDD_{186}$ motif is conserved and located at the palm domain of HIV reverse transcriptase. Mutagenesis of residues 185 and 186 from aspartate to alanine abolishes RT catalytic activity and infectivity of released virions [35]. In vitro analysis of the virions with this inactivating mutation, $D_{185}A$ and $D_{186}A$, suggested that the cores released from these virions were more stable [36]. A number of factors are involved in tuning the stability of the cores and capsid stability and reverse transcription are suggested to be balanced to minimize the innate immune sensing of HIV [37]. Atomic force microscopy measurements also suggest stages of core stiffness spikes linked to reverse transcription [38]. To our knowledge, there are no cryo-electron tomography characterizations of the cores generated

by virions with the $D_{185}A$ and $D_{186}A$ mutation in reverse transcriptase. In contrast, the mutations within the catalytic domain of integrase have been well characterized. Specifically, mutations within the catalytic domain of integrase $V_{165}A$ and $R_{166}A$, which result in inactivation of integrase, also create a phenotypic mislocalization of RNP outside of the mature cores within HIV virions. This phenotype, which can be generated by direct mutagenesis or through action of inhibitors, is defined as Type-II integrase phenotype [2,39,40].

Interaction between HIV genomic RNA (gRNA) Ψ packaging signal and the nucleocapsid (NC) domain of Gag facilitate packaging of the gRNA into budding virions [41–47]. The NC domain of Gag also has a strong affinity for cellular RNA. The absence of Ψ packaging signal within the genome significantly reduces the amount of gRNA incorporated into HIV virions in favor of more cellular mRNAs [48,49]. Within the immature virions, the gRNA primarily binds to the NC domain of Gag [47] and serves as a structural component of the virion [49]. After initiation of maturation, the gRNA also binds integrase, an interaction which is essential for proper maturation [50]; however, there is no evidence that integrase would preferentially bind a specific section of the viral gRNA. There are three sections within the signal that interact with Gag, two of them are within nucleotide 105–278 and one is within 301–332; deletion of these two sections from the gRNA($\Delta\Psi : \Delta(105–278)\&\Delta(301–332)$) abolishes Gag binding to the packaging signal but does not affect the expression of Gag from the underlying gRNA [47]. To our knowledge, there are no cryo-electron tomography characterizations of the mature cores generated by NL4.3($\Delta\Psi : \Delta(105–278)\&\Delta(301–332)$) virions.

In our study, we have used the pNL4.3 backbone, which encodes a genome derived from multiple wild type circulating group M HIV-1 viruses [51]. Transfection of the pNL4.3 backbone DNA into mammalian cells, specifically HEK293 cells, results in the release of infectious HIV-1 virions [52]. We present a quantitative method for HIV purification which allows the harvesting of 1000 to 5000 intact HIV virions from each HEK293 cell. We utilize cryo-electron tomography to compare virions produced by expression of pNL4-3(RT: $D_{185}A\&D_{186}A$) [35], NL4.3(IN: $V_{165}A\&R_{166}A$) [53], and NL4.3($\Delta\Psi : \Delta(105–278)\&\Delta(301–332)$) [47] in HEK293 cells.

2. Materials and Methods

2.1. Cell Plating and Transfections

Human embryonic kidney HEK293 cells were cultured in T-25 flasks using TrypLE Express Enzyme (Gibco, Thermo Fisher Scientific, Waltham, MA, USA) and Dulbecco's Modified Eagle Medium (DMEM) supplemented with 4 mM L-Glutamine, 4.5 g/L Glucose, sodium pyruvate (Cytiva, Marlborough, MA, USA), and 10% fetal bovine serum (Gibco). Cells were incubated at 37 °C in a humidified atmosphere containing 95% air and 5% CO_2 and passaged every other day or upon reaching confluency. Once the HEK293 cells reached 70–90% confluency, they were seeded into 10 cm culture dishes at 9 mL of medium per dish and incubated for 24 h prior to transfection. At approximately 60% confluency, cells were transfected with the designated plasmid. Unless otherwise noted, transient transfections were performed using Lipofectamine 2000 reagent (Life Technology, Carlsbad, CA, USA). For each transfection, 20 μg of plasmid DNA and 40 μL of Lipofectamine 2000 were separately diluted in 300 μL of Opti-MEM (Gibco) and incubated at room temperature for 5 min. The two solutions were then combined and allowed to incubate for an additional 20 min at room temperature to form DNA-Lipofectamine 2000 complexes. These complexes were added dropwise to each culture dish containing cells at 60% confluency. Cells were then incubated at 37 °C for 48 h before harvesting.

2.2. pNL4.3 Plasmid Preps and Mutagenesis

Cloning and plasmids: Proviral clone pNL4.3 was obtained through the NIH HIV Reagent Program, Division of AIDS, NIAID, NIH: (HIV-1), Strain NL4-3 Infectious Molecular Clone (pNL4-3), ARP-114, contributed by Dr. M. Martin. Mutagenesis resulting in pNL4-3(RT: $D_{185}A\&D_{186}A$) [35], NL4.3(IN: $V_{165}A\&R_{166}A$) [53], and NL4.3($\Delta\phi$: $\Delta(105-278)\&\Delta(301-332)$) [47] in the HIV-1 proviral clone pNL4-3 was performed by GenScript. For use in electron microscopy, an additional mutation was added to inhibit gp160 proteolysis, specifically NL4.3:Env($_{506}$SEKS$_{509}$) [54], to ensure biosafety during cryo-electron tomography.

DNA amplification and purification for transfection: A measure of 4 µg of lyophilized plasmid was resuspended in 10 µL of DNase/RNase-free distilled water and stored at −20 °C. Following this, 1 µL (0.4 µg) of each plasmid was added to 10 µL of Invitrogen MAXEfficiency chemically competent DH5α cells. Plasmid and cells were incubated on ice for 30 min and then heat shocked at 42 °C for 40 s. This was followed by a 2 min recovery on ice. Then, 250 µL of room-temperature LB was added to each tube and then plated on LB-agar plates with 0.01% ampicillin. Plates were inverted and incubated overnight at 37 °C. A single colony was used to inoculate 5 mL of LB with 10 ug/mL of ampicillin and incubated for 8 h at 37 °C whilst being shaken at 225 rpm. Then, 1 mL of this starter culture was inoculated into 500 mL liquid LB with 20 µg/mL of ampicillin and cultured overnight in a shaker (225 rpm) at 37 °C. DNA for transfections was purified per manufacturer's protocol, using the GeneJET Plasmid Maxiprep Kit (Thermo Fisher Scientific, Waltham, MA, USA), and eluted in 1 mL of elution buffer.

2.3. Preparation of OptiPrep™—Iodixanol Step Gradients

Two solutions (A and B) are prepared to make the step gradient. Solution A is made from 30 mL of 100 mM Hepes and 70 mL Phosphate-Buffered Saline (PBS). Solution B consists of 10 mL of 100 mM Hepes and 90 mL PBS. Both of these solutions are then filtered through 0.22 µm filters (CellTreat Product Code: 228747) for sterilization. Then, 10 mL of Solution A is mixed with 20 mL of OptiPrep™ Density Gradient Medium from Sigma Aldrich. This creates a solution of 40% OptiPrep™ and will be used as the bottom step in the gradient. For the top step, mix 7.5 mL of the 40% OptiPrep™ solution into 12.5 mL of Solution B to make a 15% OptiPrep™ solution.

2.4. Preparation of 10X 20 nm Gold Beads

For use with cryo-electron tomography, functionalized gold nanoparticles must be added to the resuspended pellet at the end of the purification process. 1 mL of 10 nm BSA Gold Tracers are concentrated by spinning in a 100 kD Millipore Amicon Ultra, for five minutes at 5000 rpm. Then, 1 mL of STE Buffer (20 mM TRIS-HCl, 100 mM NaCl, 1 mM EDTA, pH: 7.4) is added and spun again for 3 min. The desired final concentration is 10-fold over stock.

2.5. Freezing of Virions on EM Grids

Immediately following each VLP harvest, a one-to-one volume fraction of concentrated 10 nm gold fiducials were added to the resuspension. Then, 3.5 uL of the resulting sample was added to glow-discharged ultrathin (2 nm) carbon on Quantifoil R2/1 holey carbon film on 200 Cu mesh EM Grids (Ted Pella, Redding, CA, USA; Quantifoil Micro Tools GmbH, Großlöbichau, Germany). Following a single 2 s blot and a 1 min wait, samples were plunge-frozen in a liquid ethane/propane mix, using a Vitrobot Mark IV (Thermo Fisher Scientific), with the incubation chamber set at 4 °C and 90–100% humidity.

2.6. Cryo-Electron Tomography of Viral Particles Embedded in Vitreous Ice

Next, cryo-specimens were imaged in a Titan Krios G3i transmission electron microscope (ThermoFisher) equipped with a Gatan BioQuantum K3 energy filter and direct electron detector. Tilt series from $-60°$ to $+60°$ were recorded at $3°$ steps over holes in the carbon film via SerialEM software, version (p. 5) (University of Colorado, Boulder, CO 80309, USA) [55]. The microscope was operated at 300 kV, with images having a pixel size corresponding to 1.4 Å at the specimen. The slit width of the energy filter was 20–30 eV. Tilt series were recorded at a target defocus of -5 μm. The total electron dose at the specimen was 100–125 electrons per square Å.

2.7. Data Analysis and Tomogram Reconstruction

To generate tilt series stacks from the raw micrographs, 4–10 frames per tilt angle were automatically aligned using SerialEM. The resulting 41-frame tilt series were aligned using 10–20 gold fiducials per tilt series in IMOD (University of Colorado, Boulder, CO 80309, USA). Using IMOD, each tilt series was then fitted for CTF correction, using Ctfplotter, and dose filtered at 80% of standard. Tomograms were then 3D CTF corrected and reconstructed in 15 nm slabs for final reconstructions of 1000–1800 slices or ~140–250 nm total thickness.

2.8. Measurement of Virion Retention on Blotted Grids

A 3.5 μL aliquot of a single-cycle pseudotyped HIV-1 sample (pBR4-3IeGEnv + Vsv-g) was applied to cryo-EM grids. The grids were blotted using a Vitrobot under the same conditions described for viral-like particles (VLPs) and immediately submerged in 125 μL of supplemented DMEM within a 96-well plate. Unblotted grids, which received the same volume of the sample, served as controls. Serial dilutions of the initial volume were prepared, and the media was transferred to plates containing confluent TZM-bl cells. The cells were incubated for 48 h and subsequently stained with X-gal staining solution to quantify infectious virus particles remaining on the grids after blotting. Infectious virus titers were calculated by manually counting blue foci in the wells, then multiplying the counts by the reciprocal of the dilution factor, as previously described [56].

3. Results

3.1. Calculating an Efficient Purification Protocol for HIV Virions

The population of HIV-1 virions produced in this study likely range in durability. To maximize virion survival in this purification protocol, our goal was to remove the virions from the supernatant with minimal applied forces. For these reasons, we chose to simulate centrifugation steps to optimize purification conditions. The simulation models are presented for two condition sets. The first set conditions for an SW41 rotor with a 13 mL centrifuge tube, which can easily accommodate the 9 mL supernatant from each 10 cm plate and the two layers of Optiprep. These densities were set at 15% and 40% Optiprep.

Purification parameters for centrifugation speed, centrifugation time, and appropriate media viscosity were tuned using a custom MATLAB (2021b) script which simulated concentration and apparent force on the virions; the script is deposited online at (https://github.com/saveez/SaffarianLab, 1 January 2025). Virion concentration was modeled at discretized centrifugal radii, and changes to those concentrations were simulated over time using a finite difference method. At a given radius, the instantaneous particle velocity was estimated using Stoke's law, $v = \frac{d^2(p-L)g}{18n}$. This velocity depends on the density and viscosity of the medium at that radius and the centrifugation speed. To estimate the force exerted on the virions at a particular radius, we combined this velocity with the corresponding instantaneous viscosity using the equation $f = 2\mu r v$. To simulate virion concentration changes over time, we calculated the instantaneous Diffusion Coefficient of

the particles using the Stokes–Einstein equation, $D = \frac{kT}{6\pi\mu r}$, and iterated those concentration changes with the finite difference method.

Using our simulation, we show that running the centrifuge at 30,000 rpm, which has an average G force of 154,000 g, will collect the virions at the 15% to 40% OptiPrep solution interface within a half hour, as seen in Figure 1. The apparent force experienced by the particles, which is a function of centrifugal radius and medium viscosity, is also plotted in Figure 1. For convenience, distances are reported from the top of the buffer in the centrifuge tube at 0 and a maximum at the bottom of the tube; however, in the actual calculations, distances used are distances to the center of the rotor. Maximum forces applied to particles are predicted to hit maximum immediately before they cross the gradient boundary into 15% Opti, which would peak at ~3 fN for HIV virions with a density of 1.16 and a diameter of 140 nm. Once virions reach the interface between 15% and 40% Optiprep, the applied forces on the virions are zero.
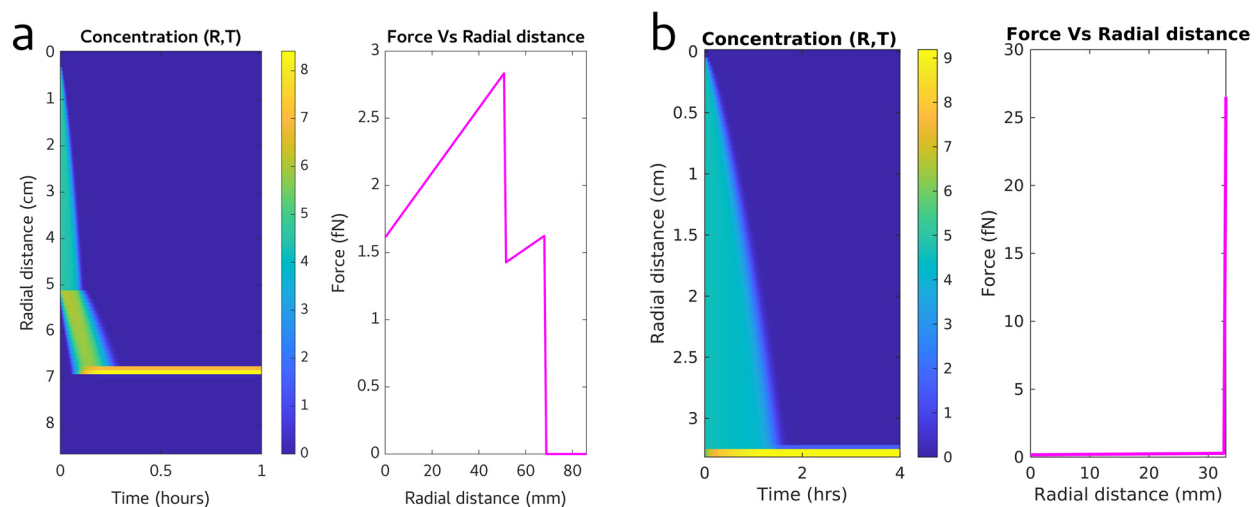

Figure 1. (**a**) Simulated concentration vs. time and force vs. radial distance data for VLPs spun at 154,000 g over a 15–40% OptiPrep™ step gradient. (**b**) Simulated concentration vs. time and force vs. radial distance data for VLPs pelleted at 20,000 g.

After extraction of the virion band, virions are embedded in the Optiprep buffer which matches their density. By diluting the virions in PBS, one can adjust the density of the surroundings and allow for additional centrifugation to pellet the virions. We hypothesized that virion damage occurs due to the total force applied to the virion multiplied by the time the virions spend under this force. If one just dilutes the virions into a large volume, the required centrifuge speed and time for pelleting will increase, and therefore, the pelleted virions will have a higher likelihood to be damaged. As shown in Figure 1 column b, the forces applied to virions in the pellet can exceed 10 times the force experienced in the first round of centrifugation, which is a substantial amount of force. To minimize this pelleting force, we used a 3× dilution of the virion band in PBS as our working solution. This dilution allows the collected viral band and dilution to be accommodated in a 1.5 mL centrifuge tube and, as shown by the calculations in Figure 1, allows for pelleting of the virions within 2 h at 20,000 g. The forces applied to virions at the bottom of the tube were calculated at below 30 fN, according to the force equation $f = \frac{4\pi r^3 (p-L)wr_{max}}{3}$. To minimize virion damage as the particles pellet against the rigid centrifuge tube, we limited pelleting time to 2 h, as is sufficient time for concentration according to calculations in Figure 1b.

3.2. Developing the Experimental Method for Virion Purification

Based on the calculation presented above, we developed the below protocol for purification, as shown in Figure 2.
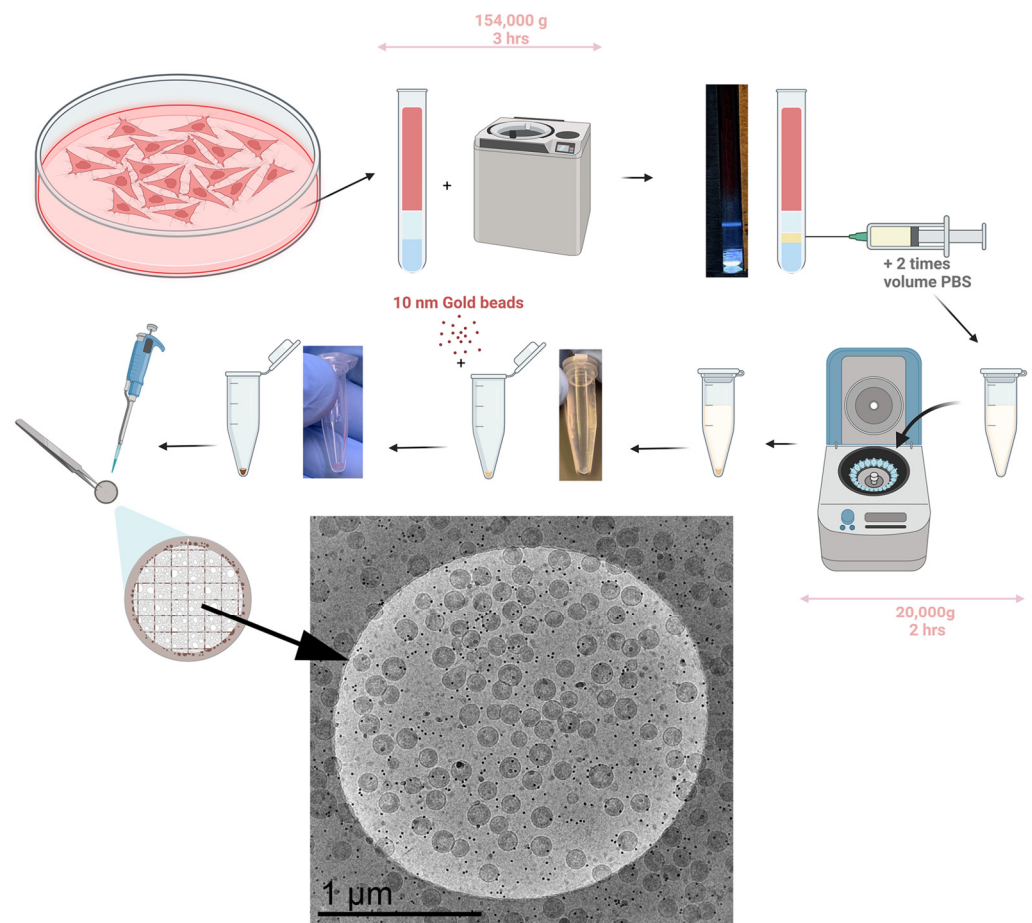

Figure 2. Schematic illustration of HIV VLP purification method from one plate of HEK293 cells. Images showing real samples are provided after the step-gradient centrifugation step, the pellet centrifugation step, and after adding the gold nanoparticles. The final image shows a 2 µm diameter circle from the final cryo-em grid.

At 48 h post-transfection, the cells and media are removed from their plates, placed in individual 15 mL tubes, and spun down at 5000 rpm for 10 min at 4° Celsius to pellet any cell debris. Then, the supernatant is filtered through 0.22 µm filters and into Ultra-Clear™ Centrifuge Tubes from Beckman Coulter (Size: 14 × 89 mm). Using a 10 mL syringe with a long stainless steel loading needle, 2 mL of 15% Opti Solution is very carefully added to the bottom of each centrifuge tube to create the first layer of the step gradient. The syringe and loading needle are cleaned with DI water and the previous step is repeated with the 40% Opti Solution to create the second (lower) layer of the gradient. The tubes are then balanced and spun at 30,000 rpm (154,000 g) for three hours at 4° Celsius.

After the spin is performed, the tubes are removed and illuminated from the bottom with a custom in-house tube holder to check the quality of the virion band: for details, see Figure S1. The band should be clearly visible against a dark backdrop and should have reasonably discrete edges. 0.5 mL of the virion band is then slowly removed by puncturing the side of the centrifuge tube with a 20 G hypodermic needle and syringe (in our study, virions used were non-infectious, to perform this experiment with infectious virions, a detailed biosafety protocol needs to be developed in collaboration with the local biosafety officers. In principle, a method based on the removal of liquids from the top of the tube

can be used in place of the needle and syringe extraction). If there are multiple tubes with the same experimental conditions, the extracted bands may be combined at this time for a higher final yield, as shown in Figure S2. The resulting volume of extracted virion band is then tripled by the addition of PBS and subsequently spun to pellet virions. As shown in Figure 2, virions resulting from one 10 cm plate will be harvested in 0.5 mL, which after adding 1 mL of PBS can be spun at 20,000 g for 2 h at 4° Celsius. After this spin, the tubes are decanted into bleach and carefully dried, taking care not to dry the pellet, which should be visible as shown in Figure 2. Depending on the final desired concentration, an amount of STE Buffer (20 mM TRIS-HCl, 100 mM NaCl, 1 mM EDTA, pH: 7.4) will be introduced to the pellet. This will have to be pipetted up and down to carefully resuspend the pellet. Once the pellet has been successfully resuspended, a one-to-one volume of $10\times$ concentrated gold beads in STE buffer is added before preparation of the EM grids. Figure 2 shows the purification of virions from HEK293 cells transfected with pNL4-3($D_{25}N$)(ΔENV) which has an inactivating $D_{25}N$ inactivating protease [57] and a frameshifting mutation which compromises the gp160 translation. Virions shown in the figure are from one 10 cm plate prepared according to protocol shown in the figure.

3.3. Measuring the Virion Yield in the Purification Protocol

To measure virion yield from our purification protocol, virion concentrations were extrapolated from tomograms and single capture Cryo-EM images of larger grid areas. Figure 2 shows a 1 μm radius circle of our Cryo-EM grid and ~120 VLPs per 1 μm radius mesh circle are visible across the sample. Tomograms show an ice thickness of 140–200 nm. To measure the fraction of virions removed from the grid during blotting, we applied 3 μL of a viral sample with known infectivity and measured the infectivity of the sample left on the grid after blotting. These measurements, as shown in Figure S3, show a 97% reduction in infectivity after blotting. Assuming a 200 nm of vitreous ice coating on both sides of the grid, the calculated volume of liquid left on the grid is 99.92% of the applied sample. According to these calculations and measurements blotting concentrates virions onto the grid by a factor of ~(1–0.97)/(1–0.9992) = 30-fold, most likely because virions adhere to the grid before blotting. By applying this factor to our calculations, we estimate that there are $10^{12}/30$ virions released from cells in a 10 cm plate. Assuming a standard 8.8×10^6 cells on a confluent 10 cm dish, this upper estimate would suggest a yield of 3800 VLPs per cell. Given uncertainty in the estimation of the thickness of ice on areas away from the holes, we estimate that the number of virions per cell are between 1000 and 5000 VLPs/Cell. In terms of a standard 3 mm Cryo-EM grid, a single 10 cm plate of confluent HEK293 cells yields a nearly complete single layer of virions for imaging using this method.

3.4. Cryo-Electron Tomographic Reconstruction of NL4.3:Env($_{506}$SEKS$_{509}$) Virions

Utilizing the above methods, we imaged virions derived from NL4.3:Env($_{506}$SEKS$_{509}$). These virions are assembled from proviral DNA with identical sequence to NL4.3, except for a mutation at the cleavage site of the gp160 ($_{506}$SEKS$_{509}$) which abrogates the cleavage of gp160, therefore causing virions to be released with intact gp160 in place of gp40/gp120 [51]. We chose this mutation primarily because it lies within gp160 which is exposed on the outside of the virions; therefore, it will have minimal impact on the maturation of HIV virions while making the released non-infectious and safe to handle in cryo-electron tomography. Figure 3 reveals three phenotypes observed in virions released from the NL4.3:Env($_{506}$SEKS$_{509}$).
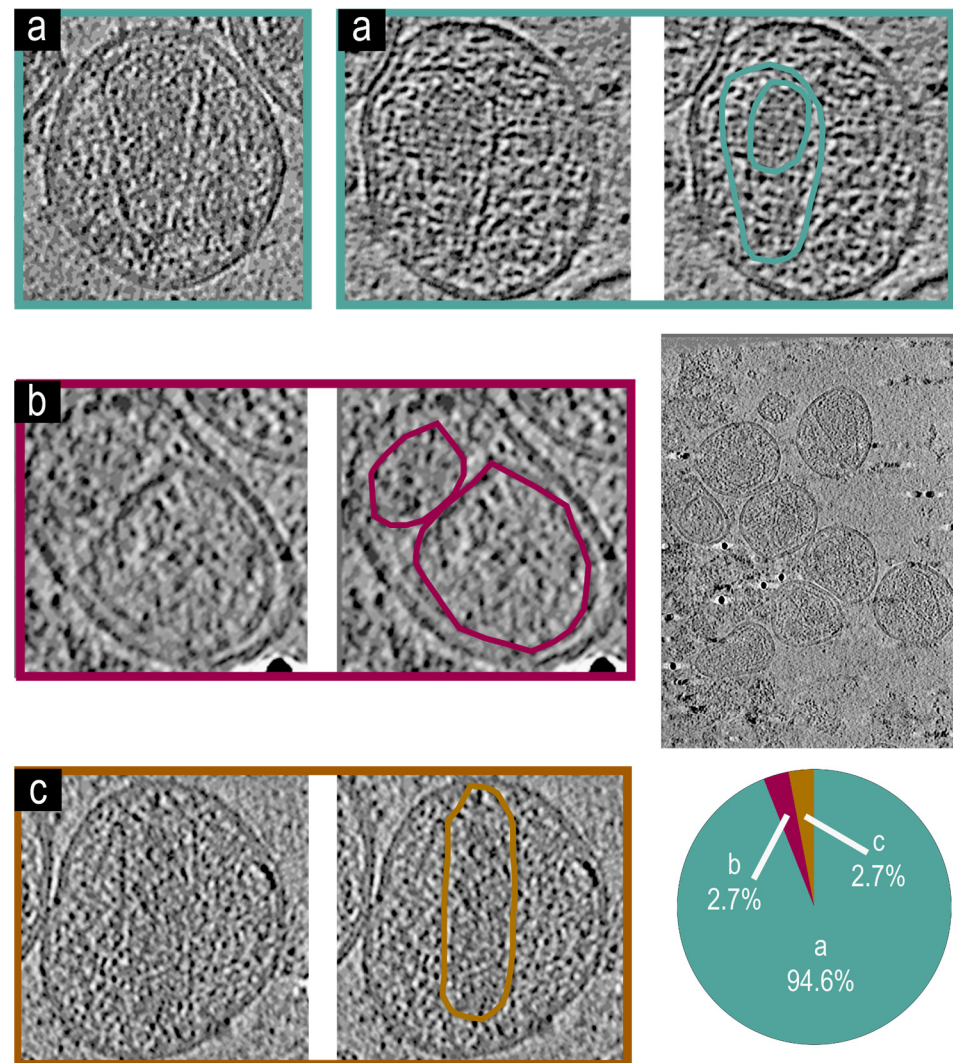
Figure 3. Representative tomogram slices from NL4.3:Env($_{506}$SEKS$_{509}$) virions. A large tomogram slice with multiple VLPs and a pie chart showing a, b and c phenotypic representation percentages is shown. Two examples of phenotype (**a**) are shown by tomogram slices of VLPs showing an intact mature core and encapsidated density, both of which are highlighted in teal for the second VLP. An example of phenotype (**b**) shows an irregular core and non-encapsidated density, both of which are highlighted in magenta. A tomogram slice of a VLP showing the phenotype (**c**) with a cylindrical core and encapsidated density, both of which are highlighted in dark yellow. (n = 54) Virions analyzed for the figure.

Figure 3a Virions with an intact mature core and encapsidated density. Figure 3b Virions with irregular core and non-encapsidated density. Figure 3c Virions with an irregular core and encapsidated density. In comparison, 95% of analyzed virions (n = 54) were type a with intact conical cores with encapsidated density. Less than 5% of virions were in either the type Figure 3b or type Figure 3c category. These results are similar to previously observed phenotypes for mature cores observed using cryo-electron microscopy measurements [14].

3.5. Cryo-Electron Tomographic Reconstruction of NL4.3($\Delta\Psi$: Δ(105–278)&Δ(301–332)) Virions

Utilizing the methods developed above, we first characterized virions generated from the NL4.3($\Delta\Psi$: Δ(105–278)&Δ(301–332)) [47]. This backbone produced three distinct phenotypes, two of which were previously characterized:

Virions with an intact mature core phenotype Figure 4a and encapsidated density. Virions with an irregular core and non-encapsidated density phenotype Figure 4b, which were previously identified in addition a new phenotype Figure 4d which is observed which shows Immature virions. These phenotypes are represented in Figure 4. A total of 55% of virions analyzed had the type Figure 4a phenotype, with intact mature cores and encapsidated density. Nearly 40% of the surveyed cores (n = 51) were deformed without visible density encapsidated Figure 4b, and a small portion of the remaining virions showed no signs of proteolytic cleavage and remained immature Figure 4d; these virions appear virtually identical to protease deactivated mutants [11,12].
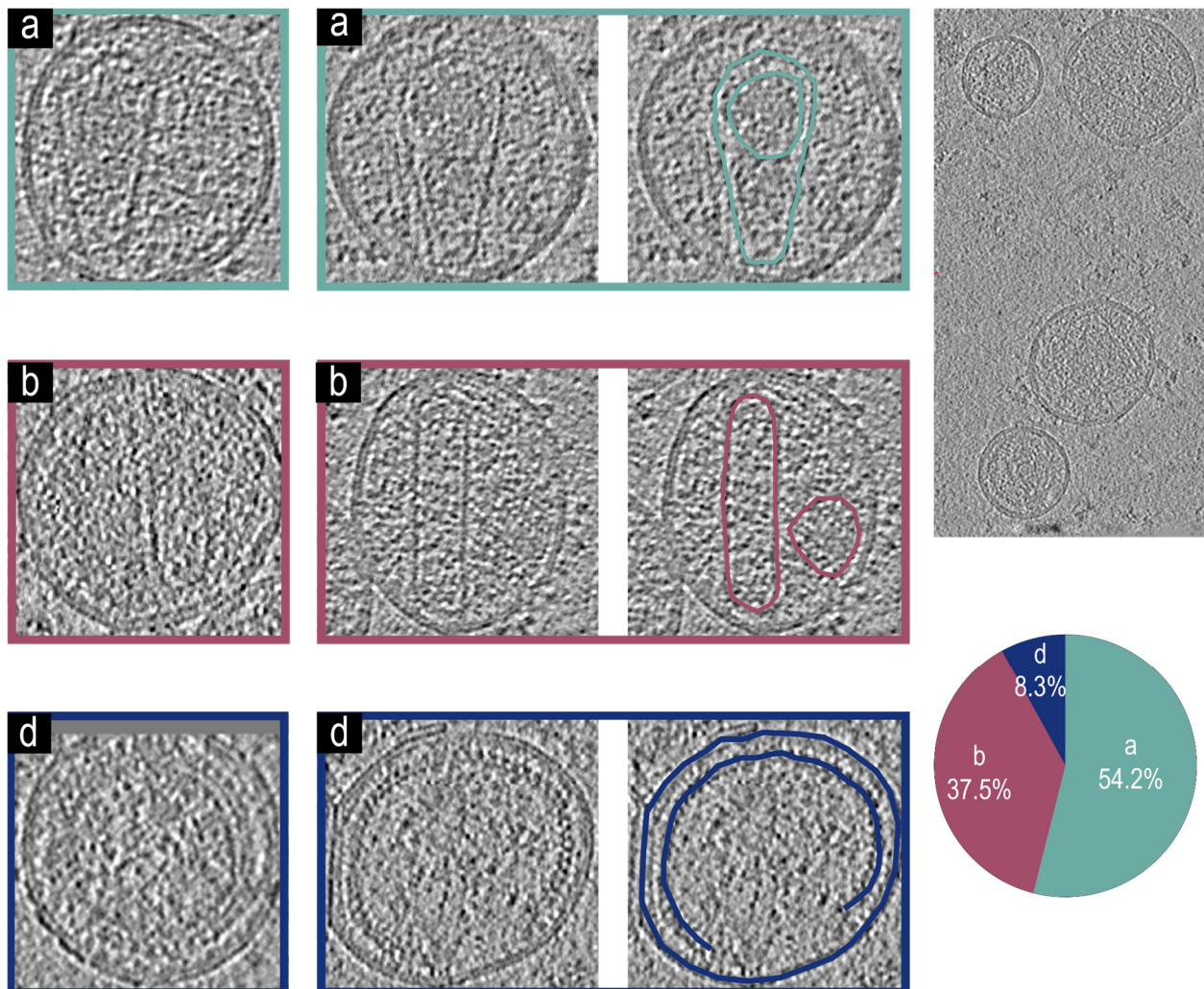

Figure 4. Representative tomogram slices from NL4.3($\Delta\Psi : \Delta(105–278)\&\Delta(301–332)$) VLPs, a larger tomogram slice with multiple VLPs, and a pie chart showing phenotypic representation percentages. Two tomogram slices of VLPs showing a phenotype (**a**) with an intact mature core and encapsidated density, both of which are highlighted in teal for the second VLP. Two tomogram slices of VLPs showing a phenotype (**b**) with an irregular core and non-encapsidated density, both of which are highlighted in magenta for the second VLP. Two tomogram slices of VLPs showing an immature phenotype (**d**) without a mature core. The immature Gag lattice and viral membrane are highlighted for the second VLP in dark blue. (n = 51) Virions analyzed for the figure.

3.6. Cryo-Electron Tomographic Reconstruction of pNL4-3(RT:$D_{185}A\&D_{186}A$)(Env($_{506}SEKS_{509}$)) Virions

It is known that interactions between integrase and the gRNA are essential for proper maturation of HIV; however, the effects of inactivating mutation of reverse transcriptase on

the core formation have not been directly observed using cryo-electron tomographic reconstruction. Figure 5 shows two major phenotypes from the NL4-3(RT: $D_{185}A\&D_{186}A$) [35] backbone: Figure 5a virions with an intact mature core and encapsidated density and Figure 5b virions with an irregular core and non-encapsidated density. We found that approximately 85% of observed virions (n = 53) had a type Figure 5a phenotype with mature cores and encapsidating density, while 15% showed cores which were deformed and did not have encapsidated density.
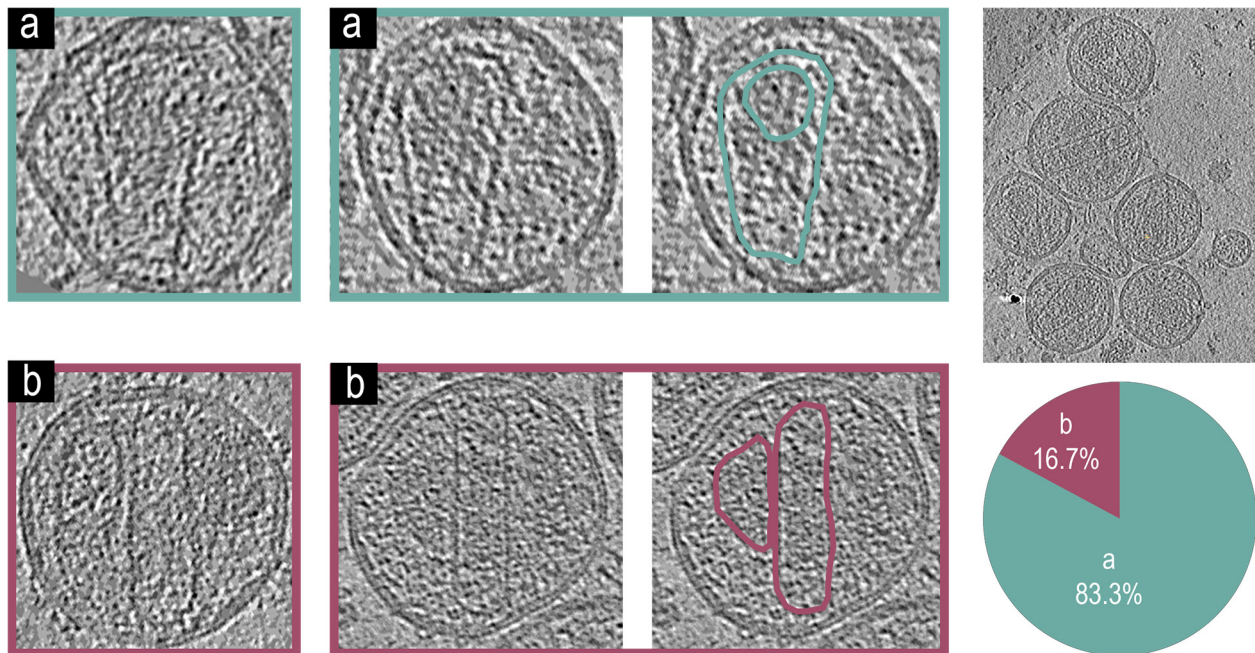

Figure 5. Representative tomogram slices from pNL4-3(RT:$D_{185}A\&D_{186}A$)(Env($_{506}$SEKS$_{509}$)) VLPs, a larger tomogram slice with multiple VLPs, and a pie chart showing phenotypic representation percentages. Two tomogram slices of VLPs showing a phenotype (**a**) with an intact mature core and encapsidated density, both of which are highlighted in teal for the second VLP. Two tomogram slices of VLPs showing a phenotype (**b**) with irregular cores and non-encapsidated density, both of which are highlighted in magenta for the second VLP. (n = 53) Virions analyzed for the figure.

3.7. Cryo-Electron Tomographic Reconstruction of NL4.3(IN: $V_{165}A\&R_{166}A$)(Env($_{506}$SEKS$_{509}$) Virions

We also examined virions from the NL4.3(IN: $V_{165}A\&R_{166}A$) [53] which has a well-known phenotype with mislocalization of RNP outside of the mature cores, defined as the Type-II integrase phenotype [2,39]. Figure 6 shows the four major phenotypes from the NL4.3(IN: $V_{165}A\&R_{166}A$) [53] backbone: Virions with an intact mature core and encapsidated density phenotype Figure 6a. Virions with an irregular core and non-encapsidated density phenotype Figure 6b. Virions without a mature core phenotype Figure 6d. Virions with a mature core and non-encapsidated density, phenotype Figure 6e. Unlike the other backbones surveyed here, the major phenotype (58%) (n = 50) of the integrase mutant was Figure 6d, which has intact cores without encapsidated density with only 10% of virions showing type Figure 6a phenotype with intact cores and detectable density inside. This major phenotype matches previous work identifying the Type-II integrase phenotype [2,39].
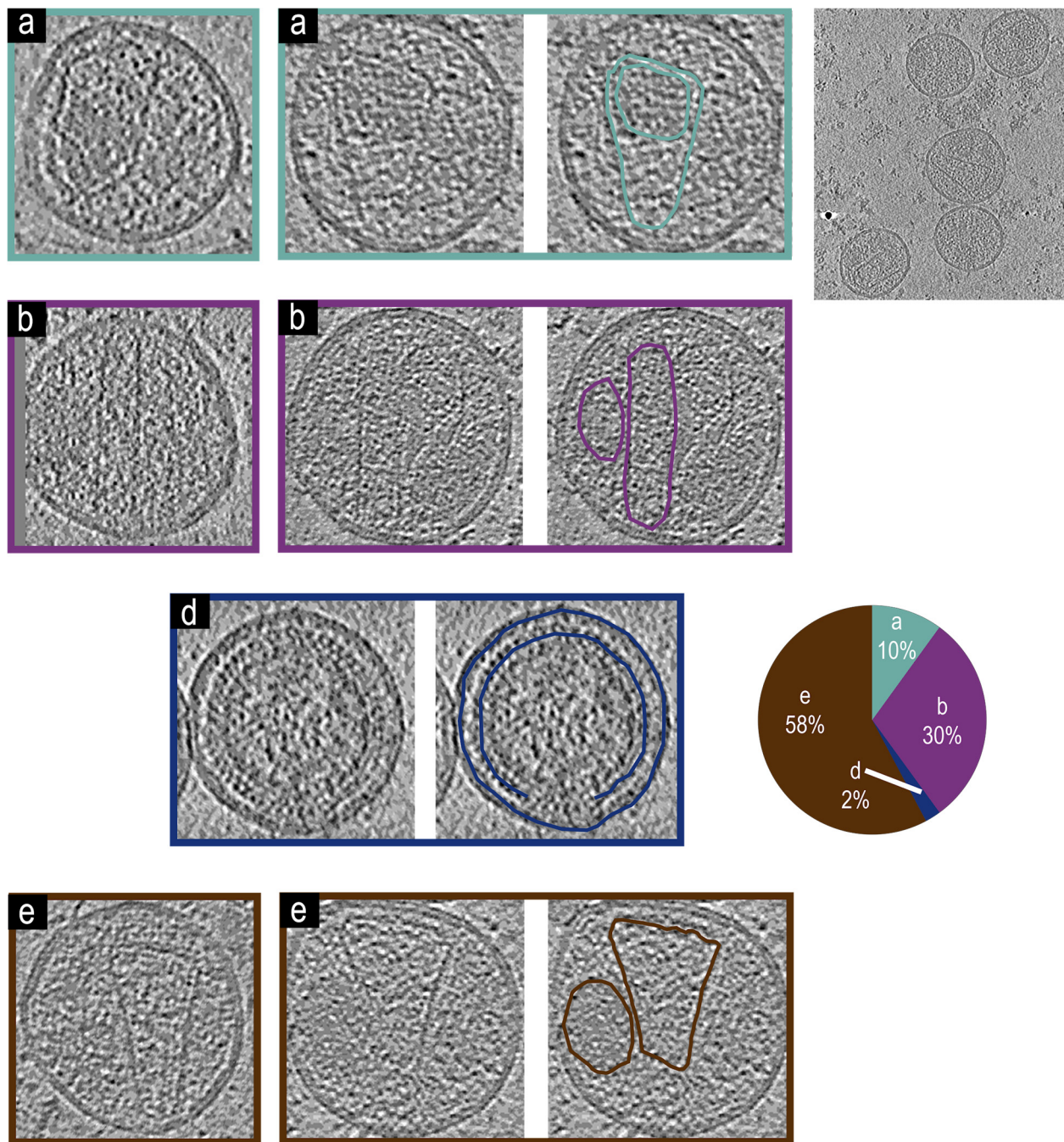
Figure 6. Representative tomogram slices from NL4.3(IN: $V_{165}A\&R_{166}A$)(Env($_{506}$SEKS$_{509}$) virions, a larger tomogram slice with multiple virions, and a pie chart showing phenotypic representation percentages. Two tomogram slices of VLPs showing phenotype (**a**) with an intact mature core and encapsidated density, both of which are highlighted in teal for the second virion. Two tomogram slices of virions showing phenotype (**b**) with an irregular core and non-encapsidated density, both of which are highlighted in magenta for the second virion. A tomogram slice of a virion showing phenotype (**d**) without a mature core. The immature Gag lattice and viral membrane are highlighted for the VLP in dark blue. Two tomogram slices of VLPs showing phenotype (**e**) with an intact mature core and non-encapsidated density, both of which are highlighted in brown for the second virion. (n = 50) Virions analyzed for the figure.

4. Discussion

Viral purification is an essential step in studying viruses, especially for analysis by cryo-electron tomography, where highly concentrated viral samples allow efficient single

particle analysis. Purifying a majority of viral particles released from cells is desirable to present a homogeneous representation of virions for structural analysis. Complex viruses like HIV are further complicated, because only 1 in 100 or 1 in 10,000 are found to be infectious [58,59]. The current manuscript is a quantitative effort to improve the virion yield and structural integrity of released virions with the goal to improve the representation of virions in analysis independent of their structural stability. The proposed protocol is also efficient and short, allowing the preparation of one cryo-EM grid of high-density virion from a 10 cm dish of HEK293 cells producing HIV virions from NL4.3 backbone within as little as 6 h (see Figure 2). The simulations can also be used to predict forces and sedimentation times for other methods, as shown in Figure S4. We also like to point out that the simulations of sedimentation and force generation used to develop a method for mature HIV virion purification can easily be adapted to purify other virions, especially some virions which have a more fragile structural integrity, for example, SARS-CoV-2 VLPs [60–63].

In our estimate of virion purification, we arrive at 1000–5000 virions released from individual HEK293 cells. It is important to discuss the approximations we used to arrive at this number. We measure the density of virions which are captured at the end of the protocol in vitreous ice on electron microscopy grids, where we could also measure the thickness of the vitreous ice using tomographic analysis of the sample. As mentioned in the results, we also estimated how virions became concentrated during blotting by estimating the thickness of the vitreous ice remaining on the grids and comparing this with the loss of infectivity accompanying the blotting process to arrive at an approximately 30-fold concentration enhancement of virions during the blotting process; because we do not have accurate data on the thickness of the ice away from the observable areas in the grid, we had to make assumptions which resulted in our higher and lower bounds of 1000 and 5000.

The release of the virions is catalyzed by endosomal sorting complexes required for transport (ESCRTs) [24,33,64–70]. The released virions are immature, with a distinct lattice of Gag molecules underpinning the inner leaflet of the virions [11,12]. HIV maturation is catalyzed by the active protease dimer [28], which needs to form by releasing the protease monomers embedded within the Pol portion of the Gag-Pol within the lumen of immature virions [2,71]. What regulates Gag-Pol auto-processing and where the Gag-Pol proteins are located within the lattice of the immature virions remains unknown. HIV maturation and protease activation coincide with release of the virions and over packaging of Gag-Pol or delay in release of the virions results in premature activation of the protease and release of non-infectious virions [72,73].

How does the release of 5000 virions per HEK293 cells compare with previously measured yields? Experiments with Rous Sarcoma Virus have shown that during active infection of cultures, cells can dedicate approximately 1% of their total protein synthesis to producing RSV virions [4]. Here, we will derive a back of the envelope comparison to HEK293 cells. In their growth phase, HEK293 cells double every 24 h, and therefore cells are capable of producing an equal mass of their biological material in 24 h. HEK293 cells have a mass of 5×10^{-10} g [74], and the mass of a single HIV virion is 10^{-18} g; therefore, the upper bound estimate of HIV production cannot exceed 10^6 virions per cell. We estimated harvesting 5×10^3–1×10^4 virions per HEK293 cell, which would be approximately 0.5–0.1% of their biomass production, respectively. These numbers are in reasonable agreement with measurements of RSV production.

We used this method of purification to analyze virions released from HEK293 cells transfected with pNL4-3(RT: $D_{185}A$ and $D_{186}A$) [35], NL4.3(IN: $V_{165}A$ and $R_{166}A$) [53] and NL4.3($\Delta\Psi$: Δ(105–278)&Δ(301–332)) [47]. Virions released from NL4.3(IN: $V_{165}A$ and $R_{166}A$) have been previously analyzed and identified with type-II integrase pheno-

type which we have reproduced in our data. The observation that virions released from NL4.3(IN: $V_{165}A\&R_{166}A$) have intact cores with RNP inside, is new, but not surprising, since to our knowledge, there are no other data suggesting that RT plays a role in core formation. The mix phenotype observed with NL4.3($\Delta\Psi : \Delta(105-278)\&\Delta(301-332)$) is, however, perplexing, partly because of observation of immature virions. The virions generated for this experiment are assembled in HEK293 cells from a single proviral DNA missing only the two sections of nucleotides which represent the φ packaging signal and therefore we expect any cell that would express Gag would also express Gag-Pol, with both Gag and Gag-Pol proteins incorporating within virions with similar ratios, as observed from the parental NL4.3 backbone. If there are Gag-Pol's incorporated within these virions, then some of the virions being immature is perplexing. Previously, it has been suggested that incorporation of Gag-Pol's is dependent on incorporation of gRNA [75], which can explain our observation, however in this study we do not provide any additional evidence and so this remains speculative.

Supplementary Materials: The following supporting information can be downloaded at: https://www.mdpi.com/article/10.3390/v17030364/s1, Figure S1: Device constructed for extraction of viral bands from the step gradients. Figure S2: For Purification Schematic. Figure S3: Measure of virions left in the grid after blotting. Figure S4: After separation of cells from supernatant, virus-particle-containing supernatants are concentrated by centrifugation through a 20% sucrose cushion at $100,000\times g$ for 2 h. Our simulation shows this centrifugation using an SW41 Ti rotor.

Institutional Review Board Statement: Not applicable.

Informed Consent Statement: Not applicable.

Data Availability Statement: The raw data supporting the conclusions of this article will be made available by the authors on request.

Conflicts of Interest: The authors declare no conflicts of interest.

References

1. Gao, F.; Bailes, E.; Robertson, D.L.; Chen, Y.; Rodenburg, C.M.; Michael, S.F.; Cummins, L.B.; Arthur, L.O.; Peeters, M.; Shaw, G.M.; et al. Origin of HIV-1 in the Chimpanzee Pan Troglodytes Troglodytes. *Nature* **1999**, *397*, 436–441. [CrossRef]
2. Knipe, D.M.; Howley, P.M.; Griffin, D.E.; Lamb, R.A.; Martin, M.A.; Roizman, B.; Straus, S.E. (Eds.) *Field's Virology*, 5th ed.; Lippincott Williams & Wilkins: London, UK, 2007.
3. Santiago, M.L.; Range, F.; Keele, B.F.; Li, Y.Y.; Bailes, E.; Bibollet-Ruche, F.; Fruteau, C.; Noë, R.; Peeters, M.; Brookfield, J.F.Y.; et al. Simian Immunodeficiency Virus Infection in Free-Ranging Sooty Mangabeys (Cercocebus Atys Atys) from the Taï Forest, Côte d'Ivoire: Implications for the Origin of Epidemic Human Immunodeficiency Virus Type 2. *J. Virol.* **2005**, *79*, 12515–12527. [CrossRef]
4. Coffin, J.M.; Hughes, S.H.; Varmus, H. (Eds.) *Retroviruses*; Cold Spring Harbor Laboratory Press: Plainview, NY, USA, 1997; ISBN 978-0-87969-571-2.

5. Mendonça, L.; Sun, D.; Ning, J.; Liu, J.; Kotecha, A.; Olek, M.; Frosio, T.; Fu, X.; Himes, B.A.; Kleinpeter, A.B.; et al. CryoET Structures of Immature HIV Gag Reveal Six-Helix Bundle. *Commun. Biol.* **2021**, *4*, 481. [CrossRef]

6. Dettenhofer, M.; Yu, X.-F. Highly Purified Human Immunodeficiency Virus Type 1 Reveals a Virtual Absence of Vif in Virions. *J. Virol.* **1999**, *73*, 1460. [CrossRef]

7. Kleinpeter, A.B.; Zhu, Y.; Mallery, D.L.; Ablan, S.D.; Chen, L.; Hardenbrook, N.; Saiardi, A.; James, L.C.; Zhang, P.; Freed, E.O. The Effect of Inositol Hexakisphosphate on HIV-1 Particle Production and Infectivity Can Be Modulated by Mutations That Affect the Stability of the Immature Gag Lattice. *J. Mol. Biol.* **2023**, *435*, 168037. [CrossRef]

8. Talledge, N.; Yang, H.; Shi, K.; Coray, R.; Yu, G.; Arndt, W.G.; Meng, S.; Baxter, G.C.; Mendonça, L.M.; Castaño-Díez, D.; et al. HIV-2 Immature Particle Morphology Provides Insights into Gag Lattice Stability and Virus Maturation. *J. Mol. Biol.* **2023**, *435*, 168143. [CrossRef]

9. Naldini, L.; Blömer, U.; Gallay, P.; Ory, D.; Mulligan, R.; Gage, F.H.; Verma, I.M.; Trono, D. In Vivo Gene Delivery and Stable Transduction of Nondividing Cells by a Lentiviral Vector. *Science* **1996**, *272*, 263–267. [CrossRef]

10. Soldi, M.; Sergi Sergi, L.; Unali, G.; Kerzel, T.; Cuccovillo, I.; Capasso, P.; Annoni, A.; Biffi, M.; Rancoita, P.M.V.; Cantore, A.; et al. Laboratory-Scale Lentiviral Vector Production and Purification for Enhanced Ex Vivo and In Vivo Genetic Engineering. *Mol. Ther. Methods Clin. Dev.* **2020**, *19*, 411–425. [CrossRef]

11. Wright, E.R.; Schooler, J.B.; Ding, H.J.; Kieffer, C.; Fillmore, C.; Sundquist, W.I.; Jensen, G.J. Electron Cryotomography of Immature HIV-1 Virions Reveals the Structure of the CA and SP1 Gag Shells. *EMBO J.* **2007**, *26*, 2218–2226. [CrossRef]

12. Briggs, J.A.G.; Riches, J.D.; Glass, B.; Bartonova, V.; Zanetti, G.; Kräusslich, H.-G. Structure and Assembly of Immature HIV. *Proc. Natl. Acad. Sci. USA* **2009**, *106*, 11090–11095. [CrossRef]

13. Ganser, B.K.; Li, S.; Klishko, V.Y.; Finch, J.T.; Sundquist, W.I. Assembly and Analysis of Conical Models for the HIV-1 Core. *Science* **1999**, *283*, 80–83. [CrossRef]

14. Briggs, J.A.G.; Wilk, T.; Welker, R.; Kräusslich, H.-G.; Fuller, S.D. Structural Organization of Authentic, Mature HIV-1 Virions and Cores. *EMBO J.* **2003**, *22*, 1707–1715. [CrossRef]

15. Schur, F.K.M.; Obr, M.; Hagen, W.J.H.; Wan, W.; Jakobi, A.J.; Kirkpatrick, J.M.; Sachse, C.; Kräusslich, H.-G.; Briggs, J.A.G. An Atomic Model of HIV-1 Capsid-SP1 Reveals Structures Regulating Assembly and Maturation. *Science* **2016**, *353*, 506. [CrossRef]

16. Saad, J.S.; Miller, J.; Tai, J.; Kim, A.; Ghanam, R.H.; Summers, M.F. Structural Basis for Targeting HIV-1 Gag Proteins to the Plasma Membrane for Virus Assembly. *Proc. Natl. Acad. Sci. USA* **2006**, *103*, 11364–11369. [CrossRef]

17. Ono, A.; Ablan, S.D.; Lockett, S.J.; Nagashima, K.; Freed, E.O. Phosphatidylinositol (4,5) Bisphosphate Regulates HIV-1 Gag Targeting to the Plasma Membrane. *Proc. Natl. Acad. Sci. USA* **2004**, *101*, 14889–14894. [CrossRef]

18. Favard, C.; Chojnacki, J.; Merida, P.; Yandrapalli, N.; Mak, J.; Eggeling, C.; Muriaux, D. HIV-1 Gag Specifically Restricts PI(4,5)P2 and Cholesterol Mobility in Living Cells Creating a Nanodomain Platform for Virus Assembly. *Sci. Adv.* **2019**, *5*, eaaw8651. [CrossRef]

19. Lei, X.; Gonçalves-Carneiro, D.; Zang, T.M.; Bieniasz, P.D. Initiation of HIV-1 Gag Lattice Assembly Is Required for Recognition of the Viral Genome Packaging Signal. *eLife* **2023**, *12*, e83548. [CrossRef]

20. Duchon, A.; Santos, S.; Chen, J.; Brown, M.; Nikolaitchik, O.A.; Tai, S.; Chao, J.A.; Freed, E.O.; Pathak, V.K.; Hu, W.S.; et al. Plasma Membrane Anchoring and Gag:Gag Multimerization on Viral RNA Are Critical Properties of HIV-1 Gag Required To Mediate Efficient Genome Packaging. *mBio* **2021**, *12*, e0325421. [CrossRef]

21. Bieniasz, P.; Telesnitsky, A. Multiple, Switchable Protein:RNA Interactions Regulate Human Immunodeficiency Virus Type 1 Assembly. *Annu. Rev. Virol.* **2018**, *5*, 165–183. [CrossRef]

22. Sarni, S.; Biswas, B.; Liu, S.; Olson, E.D.; Kitzrow, J.P.; Rein, A.; Wysocki, V.H.; Musier-Forsyth, K. HIV-1 Gag Protein with or without P6 Specifically Dimerizes on the Viral RNA Packaging Signal. *J. Biol. Chem.* **2020**, *295*, 14391–14401. [CrossRef]

23. Ku, P.-I.; Miller, A.K.; Ballew, J.; Sandrin, V.; Adler, F.R.; Saffarian, S. Identification of Pauses during Formation of HIV-1 Virus Like Particles. *Biophys. J.* **2013**, *105*, 2262–2272. [CrossRef] [PubMed]

24. Jouvenet, N.; Simon, S.M.; Bieniasz, P.D. Visualizing HIV-1 Assembly. *J. Mol. Biol.* **2011**, *410*, 501–511. [CrossRef]

25. Jouvenet, N.; Simon, S.M.; Bieniasz, P.D. Imaging the Interaction of HIV-1 Genomes and Gag during Assembly of Individual Viral Particles. *Proc. Natl. Acad. Sci. USA* **2009**, *106*, 19114–19119. [CrossRef]

26. Sundquist, W.I.; Kräusslich, H.-G. HIV-1 Assembly, Budding, and Maturation. *Cold Spring Harb. Perspect. Med.* **2012**, *2*, a015420. [CrossRef]

27. Freed, E.O. HIV-1 Assembly, Release and Maturation. *Nat. Rev. Microbiol.* **2015**, *13*, 484–496. [CrossRef]

28. Lee, S.-K.; Potempa, M.; Swanstrom, R. The Choreography of HIV-1 Proteolytic Processing and Virion Assembly. *J. Biol. Chem.* **2012**, *287*, 40867–40874. [CrossRef] [PubMed]

29. Burdick, R.C.; Li, C.; Munshi, M.; Rawson, J.M.O.; Nagashima, K.; Hu, W.-S.; Pathak, V.K. HIV-1 Uncoats in the Nucleus near Sites of Integration. *Proc. Natl. Acad. Sci. USA* **2020**, *117*, 5486–5493. [CrossRef]

30. Dharan, A.; Bachmann, N.; Talley, S.; Zwikelmaier, V.; Campbell, E.M. Nuclear Pore Blockade Reveals That HIV-1 Completes Reverse Transcription and Uncoating in the Nucleus. *Nat. Microbiol.* **2020**, *5*, 1088–1095. [CrossRef]

31. Kleinpeter, A.B.; Freed, E.O. HIV-1 Maturation: Lessons Learned from Inhibitors. *Viruses* **2020**, *12*, 940. [CrossRef]

32. Sundquist, W.I.; Krug, R.M. Assemble, Replicate, Remodel and Evade. *Curr. Opin. Virol.* **2012**, *2*, a006924. [CrossRef]

33. Weissenhorn, W.; Göttlinger, H. Essential Ingredients for HIV-1 Budding. *Cell Host Microbe* **2011**, *9*, 172–174. [CrossRef] [PubMed]

34. Bieniasz, P.D. The Cell Biology of HIV-1 Virion Genesis. *Cell Host Microbe* **2009**, *5*, 550–558. [CrossRef] [PubMed]

35. Mulky, A.; Sarafianos, S.G.; Jia, Y.; Arnold, E.; Kappes, J.C. Identification of Amino Acid Residues in the Human Immunodeficiency Virus Type-1 Reverse Transcriptase Tryptophan-Repeat Motif That Are Required for Subunit Interaction Using Infectious Virions. *J. Mol. Biol.* **2005**, *349*, 673–684. [CrossRef] [PubMed]

36. Yang, Y.; Fricke, T. Diaz-Griffero Felipe Inhibition of Reverse Transcriptase Activity Increases Stability of the HIV-1 Core. *J. Virol.* **2013**, *87*, 683–687. [CrossRef]

37. Eschbach Jenna, E.; Puray-Chavez, M.; Mohammed, S.; Wang, Q.K.; Xia, M.; Huang, L.C.; Shan, L.; Kutluay Sebla, B. HIV-1 Capsid Stability and Reverse Transcription Are Finely Balanced to Minimize Sensing of Reverse Transcription Products via the cGAS-STING Pathway. *mBio* **2024**, *15*, e0034824. [CrossRef]

38. Rankovic, S.; Deshpande, A.; Harel, S.; Aiken, C. Rousso Itay HIV-1 Uncoating Occurs via a Series of Rapid Biomechanical Changes in the Core Related to Individual Stages of Reverse Transcription. *J. Virol.* **2021**, *95*, 10–1128. [CrossRef]

39. Engelman, A.; Englund, G.; Orenstein, J.M.; Martin, M.A.; Craigie, R. Multiple Effects of Mutations in Human Immunodeficiency Virus Type 1 Integrase on Viral Replication. *J. Virol.* **1995**, *69*, 2729–2736. [CrossRef]

40. Jurado, K.A.; Wang, H.; Slaughter, A.; Feng, L.; Kessl, J.J.; Koh, Y.; Wang, W.; Ballandras-Colas, A.; Patel, P.A.; Fuchs, J.R.; et al. Allosteric Integrase Inhibitor Potency Is Determined through the Inhibition of HIV-1 Particle Maturation. *Proc. Natl. Acad. Sci. USA* **2013**, *110*, 8690–8695. [CrossRef]

41. Lever, A.; Gottlinger, H.; Haseltine, W.; Sodroski, J. Identification of a Sequence Required for Efficient Packaging of Human Immunodeficiency Virus Type 1 RNA into Virions. *J. Virol.* **1989**, *63*, 4085–4087. [CrossRef]

42. Luban, J.; Goff, S.P. Binding of Human Immunodeficiency Virus Type 1 (HIV-1) RNA to Recombinant HIV-1 Gag Polyprotein. *J. Virol.* **1991**, *65*, 3203–3212. [CrossRef]

43. McCann, E.M.; Lever, A.M. Location of Cis-Acting Signals Important for RNA Encapsidation in the Leader Sequence of Human Immunodeficiency Virus Type 2. *J. Virol.* **1997**, *71*, 4133–4137. [CrossRef]

44. Amarasinghe, G.K.; De Guzman, R.N.; Turner, R.B.; Chancellor, K.J.; Wu, Z.R.; Summers, M.F. NMR Structure of the HIV-1 Nucleocapsid Protein Bound to Stem-Loop SL2 of the Ψ-RNA Packaging Signal. Implications for Genome Recognition 11Edited by P. Wright. *J. Mol. Biol.* **2000**, *301*, 491–511. [CrossRef] [PubMed]

45. Keane, S.C.; Heng, X.; Lu, K.; Kharytonchyk, S.; Ramakrishnan, V.; Carter, G.; Barton, S.; Hosic, A.; Florwick, A.; Santos, J.; et al. Structure of the HIV-1 RNA Packaging Signal. *Science* **2015**, *348*, 917–921. [CrossRef]

46. Lu, K.; Heng, X.; Garyu, L.; Monti, S.; Garcia, E.L.; Kharytonchyk, S.; Dorjsuren, B.; Kulandaivel, G.; Jones, S.; Hiremath, A.; et al. NMR Detection of Structures in the HIV-1 5′-Leader RNA That Regulate Genome Packaging. *Science* **2011**, *334*, 242–245. [CrossRef]

47. Kutluay, S.B.; Zang, T.; Blanco-Melo, D.; Powell, C.; Jannain, D.; Errando, M.; Bieniasz, P.D. Global Changes in the RNA Binding Specificity of HIV-1 Gag Regulate Virion Genesis. *Cell* **2014**, *159*, 1096–1109. [CrossRef] [PubMed]

48. Rulli, S.J.; Hibbert, C.S.; Mirro, J.; Pederson, T.; Biswal, S.; Rein, A. Selective and Nonselective Packaging of Cellular RNAs in Retrovirus Particles. *J. Virol.* **2007**, *81*, 6623. [CrossRef] [PubMed]

49. Muriaux, D.; Mirro, J.; Harvin, D.; Rein, A. RNA Is a Structural Element in Retrovirus Particles. *Proc. Natl. Acad. Sci. USA* **2001**, *98*, 5246. [CrossRef]

50. Kessl, J.J.; Kutluay, S.B.; Townsend, D.; Rebensburg, S.; Slaughter, A.; Larue, R.C.; Shkriabai, N.; Bakouche, N.; Fuchs, J.R.; Bieniasz, P.D.; et al. HIV-1 Integrase Binds the Viral RNA Genome and Is Essential during Virion Morphogenesis. *Cell* **2016**, *166*, 1257–1268.e12. [CrossRef]

51. Adachi, A.; Gendelman, H.E.; Koenig, S.; Folks, T.; Willey, R.; Rabson, A.; Martin, M.A. Production of Acquired Immunodeficiency Syndrome-Associated Retrovirus in Human and Nonhuman Cells Transfected with an Infectious Molecular Clone. *J. Virol.* **1986**, *59*, 284–291. [CrossRef]

52. Montefiori, D.C. Measuring HIV Neutralization in a Luciferase Reporter Gene Assay. In *HIV Protocols*; Prasad, V.R., Kalpana, G.V., Eds.; Humana Press: Totowa, NJ, USA, 2009; pp. 395–405. ISBN 978-1-59745-170-3.

53. Ana, L.; Eric, D.; Richard, L.; Ghory Hina, Z.; Silver Pamela, A. Engelman Alan Nuclear Localization of Human Immunodeficiency Virus Type 1 Preintegration Complexes (PICs): V165A and R166A Are Pleiotropic Integrase Mutants Primarily Defective for Integration, Not PIC Nuclear Import. *J. Virol.* **2002**, *76*, 10598–10607. [CrossRef]

54. Pancera, M.; Wyatt, R. Selective Recognition of Oligomeric HIV-1 Primary Isolate Envelope Glycoproteins by Potently Neutralizing Ligands Requires Efficient Precursor Cleavage. *Virology* **2005**, *332*, 145–156. [CrossRef] [PubMed]

55. Mastronarde, D.N. Automated Electron Microscope Tomography Using Robust Prediction of Specimen Movements. *J. Struct. Biol.* **2005**, *152*, 36–51. [CrossRef]

56. Akrigg, A.; Wilkinson, G.W.G.; Angliss, S.; Greenaway, P.J. HIV-1 Indicator Cell Lines. *AIDS* **1991**, *5*, 153–158. [CrossRef]

57. Göttlinger, H.G.; Sodroski, J.G.; Haseltine, W.A. Role of Capsid Precursor Processing and Myristoylation in Morphogenesis and Infectivity of Human Immunodeficiency Virus Type 1. *Proc. Natl. Acad. Sci. USA* **1989**, *86*, 5781–5785. [CrossRef]

58. Rusert, P.; Fischer, M.; Joos, B.; Leemann, C.; Kuster, H.; Flepp, M.; Bonhoeffer, S.; Günthard, H.F.; Trkola, A. Quantification of Infectious HIV-1 Plasma Viral Load Using a Boosted in Vitro Infection Protocol. *Virology* **2004**, *326*, 113–129. [CrossRef]

59. Kimpton, J.; Emerman, M. Detection of Replication-Competent and Pseudotyped Human Immunodeficiency Virus with a Sensitive Cell Line on the Basis of Activation of an Integrated Beta-Galactosidase Gene. *J. Virol.* **1992**, *66*, 2232–2239. [CrossRef]

60. Gourdelier, M.; Swain, J.; Arone, C.; Mouttou, A.; Bracquemond, D.; Merida, P.; Saffarian, S.; Lyonnais, S.; Favard, C.; Muriaux, D. Optimized Production and Fluorescent Labeling of SARS-CoV-2 Virus-like Particles. *Sci. Rep.* **2022**, *12*, 14651. [CrossRef] [PubMed]

61. Swann, H.; Sharma, A.; Preece, B.; Peterson, A.; Eldridge, C.; Belnap, D.M.; Vershinin, M.; Saffarian, S. Minimal System for Assembly of SARS-CoV-2 Virus like Particles. *Sci. Rep.* **2020**, *10*, 21877. [CrossRef] [PubMed]

62. Atemin, A.; Ivanova, A.; Peppel, W.; Stamatov, R.; Gallegos, R.; Durden, H.; Uzunova, S.; Vershinin, M.D.; Saffarian, S.; Stoynov, S.S. Kinetic Landscape of Single Virus-like Particles Highlights the Efficacy of SARS-CoV-2 Internalization. *Viruses* **2024**, *16*, 1341. [CrossRef]

63. Sharma, A.; Preece, B.; Swann, H.; Fan, X.; McKenney, R.J.; Ori-McKenney, K.M.; Saffarian, S.; Vershinin, M.D. Structural Stability of SARS-CoV-2 Virus like Particles Degrades with Temperature. *Biochem. Biophys. Res. Commun.* **2021**, *534*, 343–346. [CrossRef]

64. Garrus, J.E.; von Schwedler, U.K.; Pornillos, O.W.; Morham, S.G.; Zavitz, K.H.; Wang, H.E.; Wettstein, D.A.; Stray, K.M.; Côté, M.; Rich, R.L.; et al. Tsg101 and the Vacuolar Protein Sorting Pathway Are Essential for HIV-1 Budding. *Cell* **2001**, *107*, 55–65. [CrossRef] [PubMed]

65. Gupta, S.; Bromley, J.; Saffarian, S. High-Speed Imaging of ESCRT Recruitment and Dynamics during HIV Virus like Particle Budding. *PLoS ONE* **2020**, *15*, e0237268. [CrossRef]

66. Gupta, S.; Bendjennat, M.; Saffarian, S. Abrogating ALIX Interactions Results in Stuttering of the ESCRT Machinery. *Viruses* **2020**, *12*, 1032. [CrossRef] [PubMed]

67. Baumgartel, V.; Ivanchenko, S.; Dupont, A.; Sergeev, M.; Wiseman, P.W.; Krausslich, H.-G.; Brauchle, C.; Muller, B.; Lamb, D.C. Live-Cell Visualization of Dynamics of HIV Budding Site Interactions with an ESCRT Component. *Nat. Cell Biol.* **2011**, *13*, 469–474. [CrossRef] [PubMed]

68. Demirov, D.G.; Orenstein, J.M.; Freed, E.O. The Late Domain of Human Immunodeficiency Virus Type 1 P6 Promotes Virus Release in a Cell Type-Dependent Manner. *J. Virol.* **2002**, *76*, 105–117. [CrossRef]

69. VerPlank, L.; Bouamr, F.; LaGrassa, T.J.; Agresta, B.; Kikonyogo, A.; Leis, J.; Carter, C.A. Tsg101, a Homologue of Ubiquitin-Conjugating (E2) Enzymes, Binds the L Domain in HIV Type 1 Pr55Gag. *Proc. Natl. Acad. Sci. USA* **2001**, *98*, 7724–7729. [CrossRef]

70. Martin-Serrano, J.; Yaravoy, A.; Perez-Caballero, D.; Bieniasz, P.D. Divergent Retroviral Late-Budding Domains Recruit Vacuolar Protein Sorting Factors by Using Alternative Adaptor Proteins. *Proc. Natl. Acad. Sci. USA* **2003**, *100*, 12414–12419. [CrossRef]

71. Garcia-Miranda, P.; Becker, J.T.; Benner, B.E.; Blume, A.; Sherer, N.M.; Butcher, S.E. Stability of HIV Frameshift Site RNA Correlates with Frameshift Efficiency and Decreased Virus Infectivity. *J. Virol.* **2016**, *90*, 6906–6917. [CrossRef]

72. Kräusslich, H.G. Human Immunodeficiency Virus Proteinase Dimer as Component of the Viral Polyprotein Prevents Particle Assembly and Viral Infectivity. *Proc. Natl. Acad. Sci. USA* **1991**, *88*, 3213–3217. [CrossRef]

73. Bendjennat, M.; Saffarian, S. The Race against Protease Activation Defines the Role of ESCRTs in HIV Budding. *PLoS Pathog.* **2016**, *12*, e1005657. [CrossRef]

74. Dietmair, S.; Hodson, M.P.; Quek, L.-E.; Timmins, N.E.; Gray, P.; Nielsen, L.K. A Multi-Omics Analysis of Recombinant Protein Production in Hek293 Cells. *PLoS ONE* **2012**, *7*, e43394. [CrossRef] [PubMed]

75. Benner, B.E.; Bruce, J.W.; Kentala, J.R.; Murray, M.; Becker, J.T.; Garcia-Miranda, P.; Ahlquist, P.; Butcher, S.E.; Sherer, N.M. Perturbing HIV-1 Ribosomal Frameshifting Frequency Reveals a Cis Preference for Gag-Pol Incorporation into Assembling Virions. *J. Virol.* **2022**, *96*, e0134921. [CrossRef] [PubMed]